ACS APPLIED MATERIALS & INTERFACES

Research Article

www.acsami.org

Combining RAFT Polymerization and Thiol–Ene Click Reaction for Core–Shell Structured Polymer@$BaTiO_3$ Nanodielectrics with High Dielectric Constant, Low Dielectric Loss, and High Energy Storage Capability

Ke Yang,[†] Xingyi Huang,*[,†] Ming Zhu,[†] Liyuan Xie,[†] Toshikatsu Tanaka,[‡] and Pingkai Jiang*[,†,§]

[†]Department of Polymer Science and Engineering, Shanghai Key Laboratory of Electrical Insulation and Thermal Aging, Shanghai Jiao Tong University, Shanghai 200240, People's Republic of China

[‡]IPS Research Center, Waseda University, Kitakyushu, Fukuoka 808-0135, Japan

[§]Shanghai Engineering Center for Material Safety of Nuclear Power Equipment, Shanghai 200240, People's Republic of China

Supporting Information

ABSTRACT: Nanodielectric materials with high dielectric constant, low dielectric loss, and high energy storage capability are highly desirable in modern electric and electronics industries. It has been proved that the preparation of core–shell structured dielectric polymer nanocomposites via "grafting from" method is an effective approach to these materials. However, by using this approach, the deep understanding of the structure–dielectric property relationship of the core–shell structured nanodielectrics has been limited because of the lack of detailed information (e.g., molecular weight, grafting density) about the macromolecules grafted onto the nanoparticle surfaces. In this work, by the combination of reversible addition–fragmentation chain transfer (RAFT) polymerization and thiol–ene click reaction, two types of core–shell structured polymer@$BaTiO_3$ (polymer@BT) nanocomposites with high dielectric constant and low dielectric loss were successfully prepared via a "grafting to" method. Compared with the "grafting from" method, this "grafting to" method has two merits: the molecular weight of the polymer chains in the shell layer can be easily controlled and the grafting density can be tailored by changing the molecular weight of the grafting polymer. Moreover, a clear insight into the relationship among the dielectric properties and energy storage capability of the core–shell structured polymer@BT nanocomposites, the molecular weight of the polymer chains, and the grafting density of the core–shell structured nanoparticles was achieved. The study provides new insights into the design and preparation of nanodielectric materials with desirable dielectric properties.

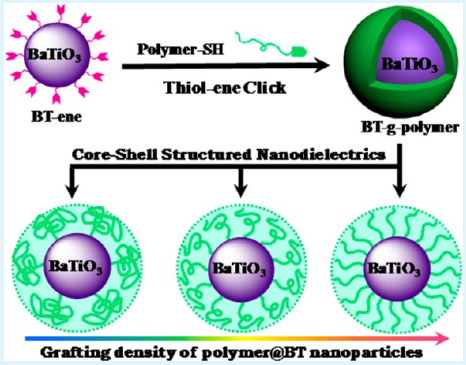

KEYWORDS: *reversible addition–fragmentation chain transfer (RAFT) polymerization, thiol–ene, click reaction, core–shell structure, nanocomposites, dielectric constant, dielectric loss, energy storage*

INTRODUCTION

Dielectric materials with high dielectric constant and low dielectric loss have received increasing interests recently for various potential applications, such as embedded capacitors, electroactive materials, and gate dielectrics.[1−4] Generally, the traditional ferroelectric ceramics (e.g., $BaTiO_3$, BT) have a high dielectric constant but are suffered from low dielectric strength and difficulties of processing. Organic polymers have flexibility, ease of processing, high dielectric strength, and low dielectric loss, but have the disadvantage of low dielectric constant (i.e., <5).[5−8] As a consequence, many efforts have been devoted to flexible materials with high dielectric constant by organic/inorganic hybrid strategy, namely, preparing composites by introducing high-dielectric-constant ceramic fillers into polymer matrices. The polymer/ceramic particulate composites combine the advantages of ceramics and polymers, presenting high dielectric constant, low dielectric loss, and ease of processing.[9−18] However, by traditional methods (e.g., melt blending or solution mixing), the realization of a high enough dielectric constant in composites needs a high loading of ceramic filler (i.e., >50 vol %),[19,20] which inevitably raises the issues of inhomogeneity and aggregation filler in the polymer matrices, resulting in deteriorated mechanical properties, high dielectric loss, and low breakdown strength.[21−23]

Recently, a promising strategy for flexible nanodielectrics with high dielectric constant and low dielectric loss has been developed by the preparation of core–shell structured nanocomposites via grafting the inorganic filler particles with polymer chains.[24−26] In such materials, the inorganic cores possess high dielectric constant, and the polymer shells are

Received: October 30, 2013
Accepted: January 7, 2014
Published: January 7, 2014

   dx.doi.org/10.1021/am4048267 | ACS Appl. Mater. Interfaces 2014, 6, 1812−1822

robust grafted onto the surface of the core, either providing strong interchain forces with matrix or acting as matrix directly.[27−31] Therefore, the volume fraction of the inorganic fillers could be maximized by reducing the fraction of host polymeric chains or completely replacing the polymer matrix by grafting polymer chains. Additionally, the inorganic fillers in core−shell structured nanocomposites could be well dispersed in a highly filled system, resulting in high dielectric constant, low dielectric loss and high dielectric strength.

It has been revealed in previous publications that there are two routes to precisely preparing core−shell structured nanodielectrics. One common protocol involves the in situ growth of the polymer chains from appropriately functionalized nanoparticles, which is known as the "grafting from" method. Through this route, a wide range of polymer chains could be grafted from the inorganic core and high grafting density could be achieved. For example, Marks and his co-workers prepared a series of core−shell structured polyolefin-based nanocomposites with high dielectric constant via in situ olefin polymerization from metallocene catalysts functionalized oxide nanoparticles.[27,28,32,33] More recently, our group successfully prepared core−shell structured PMMA@$BaTiO_3$ and PS@$BaTiO_3$ nanodielectric materials via in situ atom transfer radical polymerization (ATRP)[34] and reversible addition−fragmentation chain transfer (RAFT)[35] polymerization from the $BaTiO_3$ surface, respectively. Through in situ RAFT polymerization, we also successfully synthesized a series of core−shell structured fluoropolymer@$BaTiO_3$ nanoparticles, and the corresponding ferroelectric polymer-based nanocomposites with high dielectric constant, low dielectric loss and high energy storage density were prepared.[36]

Another effective route to prepare core−shell structured nanodielectrics is the "grafting to" method, upon which the preprepared polymer chains are grafted onto the nanoparticle surface using the affinity of the polymer end-group and the functionalities present on the surface of the particles. Such an approach is known to afford good control on the molecular composition and parameter of the attached polymer chains. For instance, in the work of Maliakal et al., core−shell structured PS@TiO_2 nanodielectric materials were prepared by ligand exchange reaction of phosphonate terminated polystyrene with oleic acid terminated TiO_2 nanoparticles.[24] Vaia and his co-workers also prepared a series of core−shell structured PS@TiO_2 nanodielectric materials by Cu(I)-catalyzed alkyne−azide click (CuAAC) chemistry.[37] However, these "grafting to" methods generally suffer from low efficiency or have metallic ion residual which is disadvantageous for the dielectric properties of the materials. Therefore, it is important to develop other more effective "grafting to" approaches to prepare core−shell structured nanodielectrics.

Thiol−ene reaction, one "click chemistry" reaction, has been proven to be a powerful and versatile synthetic technique for the preparation of functional materials,[38−41] not only because the thiol−ene reaction is highly efficient, free of byproduct, and can bind any compound with another, but also because the thiol−ene reaction does not require toxic transition metals as catalyst in comparison with CuAAC.[42,43] As consequence, the thiol−ene reaction has been widely used as a versatile tool for the preparation of organic/inorganic nanocomposites with desirable properties.[44−47] However, to the best of our knowledge, the application of the thiol−ene click reaction to prepare high-performance organic/inorganic nanodielectrics has not been reported.

In this work, we report a novel "grafting to" route to prepare core−shell structured polymer@$BaTiO_3$ nanodielectrics. Thiol-terminated PS or PMMA macromolecules with different molecular weight was first prepared by the RAFT polymerization and then a series of PS@$BaTiO_3$ and PMMA@$BaTiO_3$ nanocomposites were prepared by thiol−ene click reaction on the surface of vinyl-functionalized $BaTiO_3$ nanoparticles. The dielectric properties and the energy storage capability of the core−shell structured nanodielectrics were investigated. Moreover, a particular attention was paid to the engineering of the shell to understanding the relationship between the molecular weight of the polymer chains and the grafting density as well as the dielectric properties and energy storage capability of the resulting nanodielectrics.

EXPERIMENTAL SECTION

Materials. $BaTiO_3$ nanoparticles (the average diameter was 100 nm characterized with transmission electron microscopy) were supplied by the Shandong Sinocera Functional Material Company, China. Toluene, methanol (MeOH), ethanol, *N*,*N*-dimethylformamide (DMF), tetrahydrofuran (THF), hydrazine hydrate (85%), and other organic solvents were supplied by Shanghai Reagents Co. Ltd. Azodiisobutyronitrile (AIBN), 4-methoxyphenol (MEHQ), γ-methacryloxypropyltrimethoxysilane (MPS), styrene (St), and methyl methacrylate (MMA) were purchased from Acros. St and MMA monomers were passed through a column of Al_2O_3 to remove the inhibitor before polymerization. AIBN was recrystallized twice from methanol prior to use. The chain transfer agent (CTA) *S*-1-ethyl-*S*′-(α,α′-dimethyl-α″-acetic acid) trithiocarbonate (EDMAT) was synthesized according to the method in the literature.[48] The surface hydroxylation of $BaTiO_3$ nanoparticles (BT-OH) was conducted according to the literature method.[35] The pure PS (STYRON666H) was supplied from Dow Chemical. The pure PMMA (VH-001) was purchased from Mitsubishi Rayon Corporation.

Synthesis of Thiol-Terminated Polymer Chains via RAFT Polymerization. Thiol-terminated polystyrene (PS-SH) chains were synthesized via RAFT polymerization of St and subsequent thiol-modification. The St monomer (2.08 g, 0.02 mol), EDMAT chain transfer agent (CTA, 22.5 mg, 0.1 mmol) and AIBN initiator (5.0 mg, 0.03 mmol) were introduced into 2 mL of DMF in a 25 mL round-bottom flask. This flask was then capped with a rubber plug and the solution was deoxygenated by purging with nitrogen gas for 40 min. The mixture was stirred at 70 °C for 20 h under nitrogen atmosphere. The polymerization was stopped by quenching the flask in ice water. The reaction mixture was diluted with THF and poured into an excess volume (300 mL) of MeOH to precipitate the polymer product. The as-prepared polymer chains (PS-CTA) were further purified by two cycles of dispersion and precipitation in THF and MeOH, respectively. About 1.0 g of light yellow powder was obtained after drying the sample in a vacuum oven at room temperature for 24 h (gel permeation chromatography measurements: M_n = 10 300 g/mol, M_w/M_n = 1.22).

The thiol-modification of PS-CTA was conducted according to the literature method.[49] About 1.0 g of the PS-CTA was dispersed in 50 mL of THF. Then, about 10 μL of hydrazine hydrate was added to the polymer solution under vigorous stirring. The reaction mixture was stirred at room temperature for 30 min to ensure complete reduction of the trithiocarbonate terminal groups to thiol groups. During this period, the originally light-yellow solution turned colorless. The resultant solvent was concentrated to about 15 mL by rotary evaporation, and poured into an excess volume (300 mL) of MeOH with a small amount of acetic acid to precipitate the polymer product. The as-prepared thiol-terminated PS (PS-SH) was further purified by two cycles of dispersion and precipitation in THF and MeOH, respectively. The PS-SH was obtained as a white powder after drying the sample in a vacuum oven at room temperature for 24 h.

Scheme 1. Schematic Illustration for (A) Synthesis of Thiol-Terminated Polymer Chains via RAFT Polymerization and (B) Preparation of Core−Shell Structured Polymer@$BaTiO_3$ Nanocomposites by Thiol−Ene Click Reaction

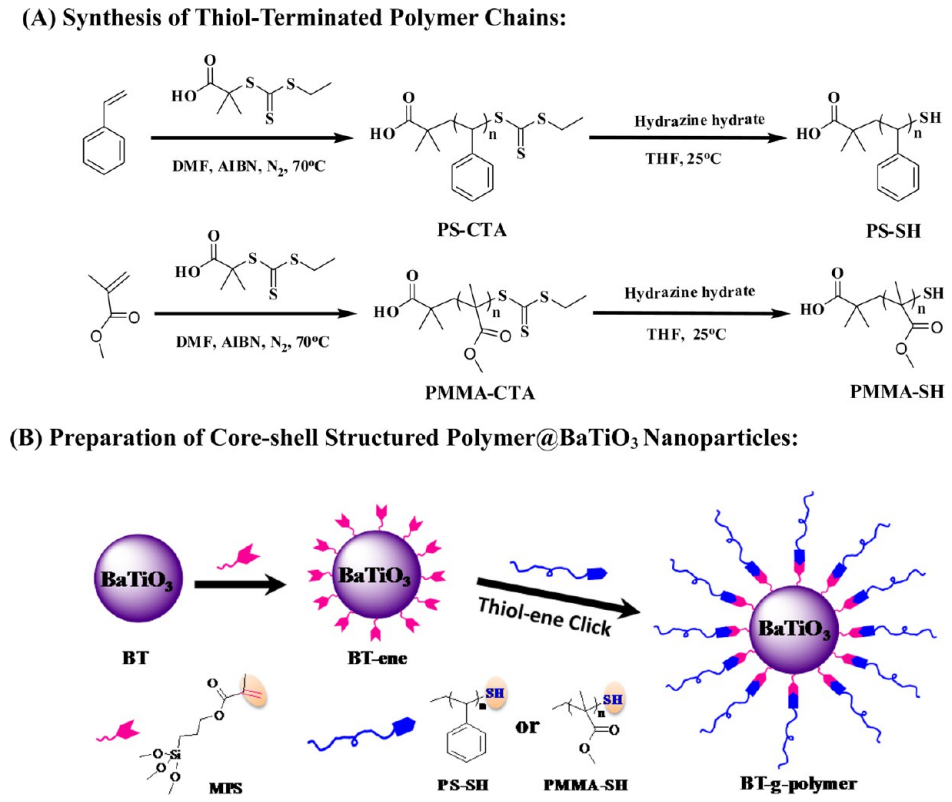

The procedures for the synthesis of thiol-terminated poly(methyl methacrylate) (PMMA-SH) chains were the same as described above, except for using MMA monomer.

Preparation of Vinyl-Functionalized $BaTiO_3$ Nanoparticles. The vinyl-functionalized $BaTiO_3$ nanoparticles (BT-ene) were prepared as follows: 10 g of BT-OH nanoparticles and 80 mL of toluene were combined in a 150 mL three-necked round-bottomed flask and sonicated for 30 min; 3 mL of MPS and 20 mg of MEHQ were added, and the mixture was heated to 80 °C for 24 h under a nitrogen atmosphere with vigorous stirring. The nanoparticles were recovered by centrifugation at 9000 rpm for 5 min and washed with ethanol twice. The obtained $BaTiO_3$ nanoparticles (BT-ene) were dried under vacuum at room temperature for 24 h.

Preparation of Core−Shell Structured Polymer@$BaTiO_3$ Nanocomposites by Thiol−Ene Click Reaction. The typical procedures for core−shell structured $BaTiO_3$ nanoparticles grafted with PS (BT-*g*-PS) by thiol−ene click reaction were prepared as follows: BT-ene nanoparticles (1.0 g), PS-SH polymer chains (0.50 g), and DMF (20 mL) were added to a 50 mL round-bottom flask followed by sonication and addition of AIBN (5.0 mg). This flask was then capped with a rubber plug, and the solution was deoxygenated by purging with nitrogen gas for 40 min. The mixture was stirred at 60 °C for 24 h under a nitrogen atmosphere. The polymerization was stopped by quenching the flask in ice water, and the $BaTiO_3$ nanocomposites were obtained by centrifugation at 9000 rpm for 15 min. The products were redispersed in toluene, and the mixture was centrifuged; this cycle was repeated three times. The BT-*g*-PS nanoparticles were dried under vacuum at 60 °C for 24 h. The samples were obtained by hot compression molding at 200 °C for 15 min.

The procedures for the preparation of core−shell structured $BaTiO_3$ nanoparticles grafted with PMMA (BT-*g*-PMMA) were the same as described above, except for using PMMA-SH polymer chains.

Characterization. X-ray diffraction patterns were collected on a powder diffractometer (D/max-2200/PC, Rigaku, Japan) using Cu Kα irradiation (40 kV, 20 mA) from 10° to 80° at a speed of 6° min^{-1}. Fourier-transform infrared (FT-IR) spectra with a Paragon 1000 (Perkin-Elmer) spectrometer and ^{1}H NMR spectra with a Varian Mercury Plus 400-MHz spectrometer were used to characterize the chemical structural of the core−shell structured polymer@BT nanoparticles. The molecular weight and polydispersity of the polymers were determined by gel permeation chromatography (GPC) analysis using THF as an eluent at a flow rate of 1.0 mL min^{-1} at 25 °C on a Perkin-Elmer 200 gel permeation chromatography instrument with a PL mixed-B10m column equipped with a reflective index detector, and the calibration was carried out with polystyrene standards. Thermogravimetric analysis (TGA) was performed using a NETZSCH TG209 F3 instrument with a heating rate of 20 °C min^{-1} in nitrogen flow (20 mL min^{-1}). The average size and size distribution of the nanoparticles were determined by dynamic light scattering (DLS) method using a Nano-ZS90 Zeta Sizer instrument (Malvern Instruments Ltd., U.K.). Transmission electron microscopy (TEM) images of the core−shell structured polymer@BT nanoparticles were obtained from a JEOL JEM-2100 instrument operated at an accelerating voltage at 160 kV. Scanning electron microscopy (SEM) images of the sample films were taken on a field-emission scanning electron microscope (JSM-7401F, JEOL, Japan) at an acceleration voltage of 5 kV. The dielectric properties of the samples were measured using a Novocontrol Alpha-N high resolution dielectric analyzer (GmbH Concept 40) at a wide range of temperatures (0−100 °C). All the measurements were carried out in the frequency range 10^{-1} to 10^6 Hz, applying 1.0 ac voltage across two opposite sides of the disk-shaped samples and a layer of gold evaporated on both surfaces to serve as electrodes. Electric displacement−electric field (D−E) loops were recorded in a Precision Premier II ferroelectric polarization tester (Radiant, Inc.) at room temperature and 10 Hz using the same samples prepared for dielectric properties testing. Polarization data were acquired for applied voltages ranging from 1 to 3999 V.

dx.doi.org/10.1021/am4048267 | ACS Appl. Mater. Interfaces 2014, 6, 1812−1822

Table 1. Characterizations of the Polymer Chains and the Resulting Core–Shell Structured Polymer@BT Nanoparticles

sample	DP of grafting polymer[a]	M_n of grafting polymer ($\times 10^3$ g/mol)[b]	M_w/M_n of grafting polymer[b]	weight loss of nanoparticles (%)[c]	grafting density of nanoparticles (chains/nm^2)[d]
BT-*g*-PS1	95	10.3	1.22	8.00	0.518
BT-*g*-PS2	396	41.6	1.16	8.79	0.145
BT-*g*-PS3	763	80.5	1.19	7.37	0.061
BT-*g*-PMMA1	98	10.7	1.20	9.21	0.585
BT-*g*-PMMA2	402	42.6	1.23	10.03	0.167
BT-*g*-PMMA3	769	81.3	1.24	8.65	0.072

[a]Calculated from ^{1}H NMR spectra of polymer-CTA. [b]Obtained from GPC results of polymer-CTA. [c]Calculated from TGA results based on the weight loss of BT-ene nanoparticles. [d]Calculated based on the M_n of grafting polymer and the weight loss of nanoparticles, considering each particle as a sphere nanoparticle with d = 100 nm.

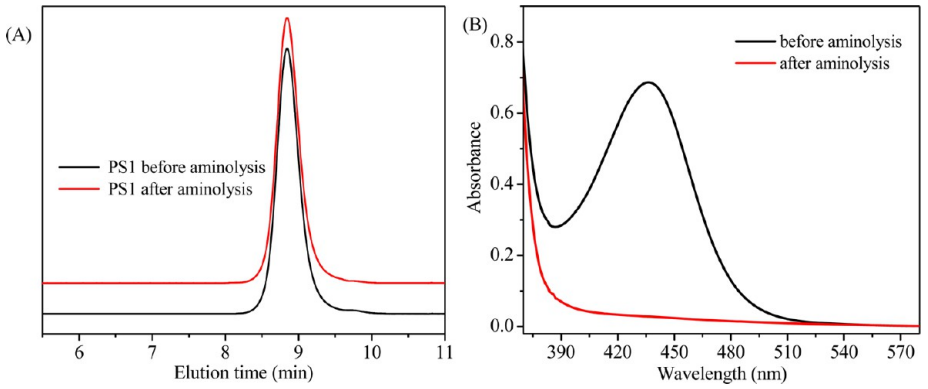

Figure 1. (A) GPC traces and (B) UV–vis spectra of PS1: before aminolysis (black) and after aminolysis (red).

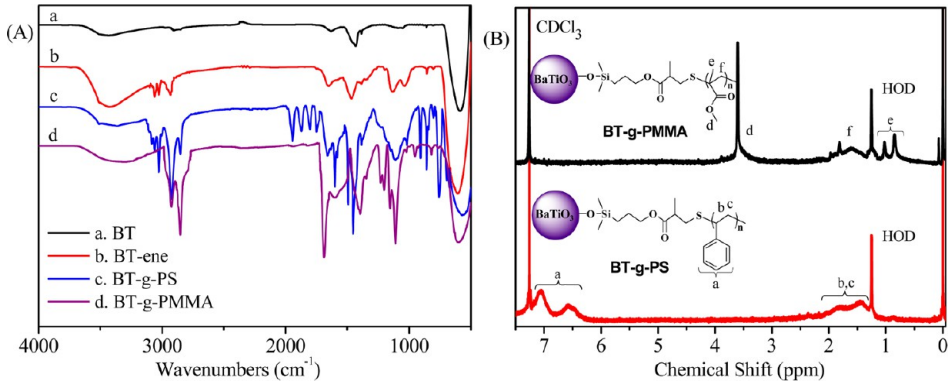

Figure 2. (A) FT-IR spectra of the as-received BT nanoparticles and surface modified BT nanoparticles; (B) ^{1}H NMR spectra of BT-*g*-PS and BT-*g*-PMMA.

RESULTS AND DISCUSSION

Preparation and Characterization of Core–Shell Structured Polymer@$BaTiO_3$ Nanocomposites. Scheme 1 shows the preparation process of thiol-terminated polymer chains (PS-SH and PMMA-SH), vinyl-functionalized $BaTiO_3$ nanoparticles (BT-ene), and core–shell structured polymer@$BaTiO_3$ nanocomposites (BT-*g*-PS and BT-*g*-PMMA). The X-ray diffraction pattern and HR-TEM image of the $BaTiO_3$ nanoparticles are collected (Figure S1 in the Supporting Information); these results show that the $BaTiO_3$ nanoparticles used in this study are tetragonal. To achieve a narrow molecular weight distribution (M_w/M_n) and precisely control the molecular weight, we employed RAFT polymerization for the synthesis of the polymers. More importantly, after RAFT polymerization, each polymer chain could contain a thioester terminal group (dithioester or trithiocarbonate), which could be transformed to thiol group by reduction or aminolysis.[50,51] Herein, two kinds of polymers, PS and PMMA, with different molecular weights and narrow molecular weight distuributions were synthesized (Scheme 1 and Table 1). Hydrazine as a highly efficient nucleophile and reductant was used to conduct the thiol-modification of polymer-CTA. It has been confirmed in previous publications that hydrazine could improve the aminolysis rate of thioester terminal group when compared with a commonly used primary amine, and produce thiol-terminated polymer chains free of disulfides even when the aminolysis was conducted in air.[49]

The polymer chains were characterized by ^{1}H NMR and GPC to determine the degree of polymerization (DP), molecular weight and molecular weight distribution. As shown in Table 1, six samples with different molecular weight for PS and PMMA were obtained, which were denoted as PS1, PS2 and PS3 for PS, and PMMA1, PMMA2 and PMMA3 for PMMA, respectively. The DP of the samples were calculated

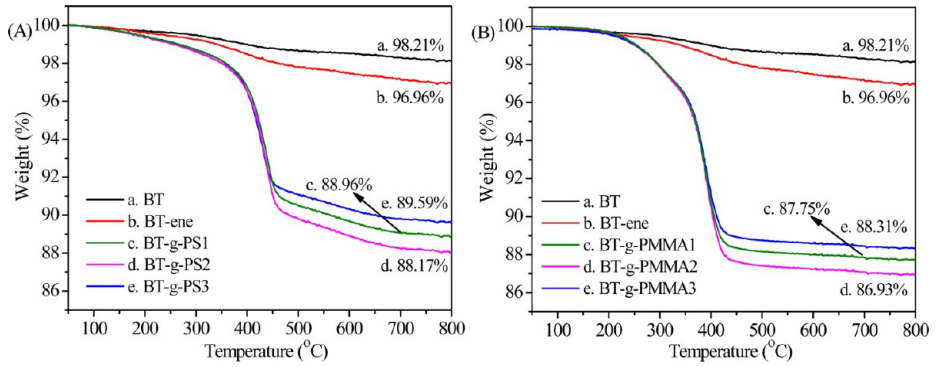

Figure 3. TGA spectra of the as-received BT nanoparticles, BT-ene, (A) BT-*g*-PS and (B) BT-*g*-PMMA.

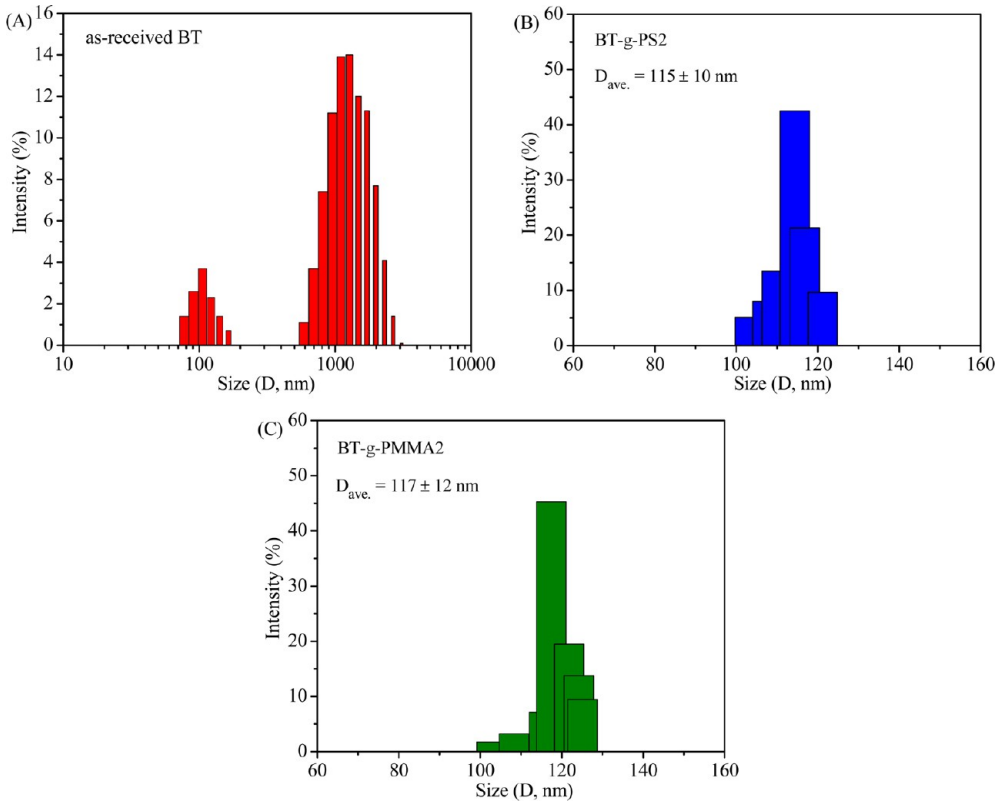

Figure 4. Particle size and distribution of the (A) as-received BT nanoparticles, (B) BT-*g*-PS2, and (C) BT-*g*-PMMA2 in toluene.

from ^{1}H NMR according to the method in the literature.[52,53] Table 1 also reports that narrow M_w/M_n values for all samples were successfully achieved. The thiol-modification of polymer-CTA was conducted by hydrazine subsequently. Figure 1A shows the GPC traces of PS1 and its polymer thiol product. It is noteworthy that, after aminolysis, the GPC trace of PS1-SH is essentially identical to the PS1 and no shoulder peak could be found, indicating that there is no formation of disulfides during the thiol-modification by hydrazine. To confirm the successful transformation of the thioester to the thiol group, the UV−vis spectra were carried out. As shown in Figure 1B, the characteristic absorption of trithiocarbonate (~430 nm) was found to disappear after aminolysis. The FT-IR spectra of the PS1 before and after aminolysis were also measured (Figure S2 in the Supporting Information). One can see that, after aminolysis, the characteristic absorption at 1223 cm^{-1} for C═S stretching disappeared, and a new absorption ascribed to -SH stretching was observed at 2580 cm^{-1}. These results confirm the complete removal of the thioester end groups and the formation of the thiol groups.[48,54]

The γ-methacryloxypropyltrimethoxysilane (MPS, Scheme 1) was immobilized onto the surface of BT nanoparticles via a hydrolysis/condensation process. The vinyl-functionalized BT nanoparticles (BT-ene) were characterized by FT-IR spectra (Figure 2A). Compared with the as-received BT nanoparticles, the new absorption bands at 1038 cm^{-1} (Si−O−Si), 1140 cm^{-1} (Si−O−BT), 1650 cm^{-1} (−C═O), 2800−3000 cm^{-1} (−CH_2, −CH_3), and 3000−3200 cm^{-1} (CH═CH_2) revealed that BT-ene was successfully prepared (line b in Figure 2A). Subsequently, the PS-SH or PMMA-SH polymer chains were grafted onto the surface of BT-ene nanoparticles by thiol−ene click reaction (Scheme 1). The FT-IR spectra of BT-*g*-PS and BT-*g*-PMMA (lines c and d in Figure 2A) show the characteristic absorption bands at 1700−2000 cm^{-1} (aromatic overtones) and 700−765 cm^{-1} (C−C bending of aromatic) for PS, 1730−1750 cm^{-1} (−C═O) and 1150−1200 cm^{-1} (−C-O)

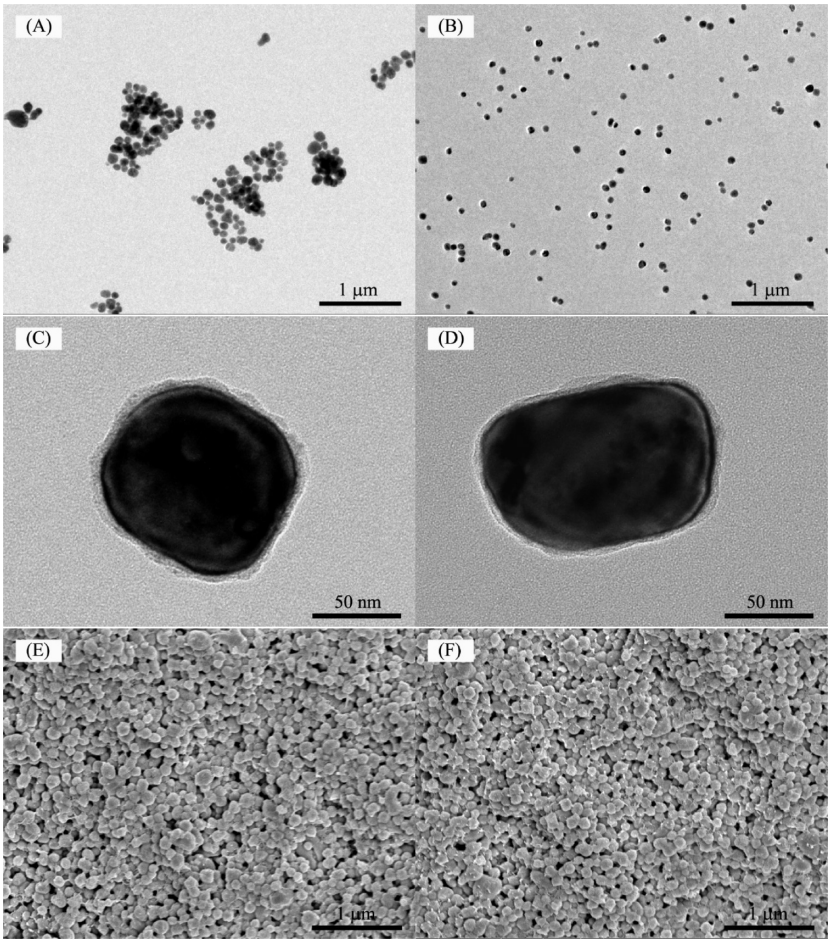

Figure 5. TEM images of the (A) as-received BT nanoparticles and (B) BT-*g*-PS2 nanoparticles at low magnification; TEM images of the (C) BT-*g*-PS2 nanoparticle and (D) BT-*g*-PMMA2 at high magnification; SEM images of the freeze-fractured cross section of the (E) BT-*g*-PS2 and (F) BT-*g*-PMMA2 nanocomposite films.

for PMMA, respectively. The ^{1}H NMR spectra of BT-*g*-PS and BT-*g*-PMMA provide more detailed evidence to prove that PS or PMMA were successfully grafted onto the surface of BT nanoparticles. As shown in Figure 2B, the characteristic proton signals at 6.21−7.45 ppm and 1.32−2.04 ppm for PS, 3.6 ppm, 1.31−2.05 ppm, and 0.63−1.15 for PMMA could be clearly detected. All these results prove that the polymer chains were successfully grafted onto the surface of the BT nanoparticles.

To determine the polymer content on the surface of functionalized BT nanoparticles, the thermogravimetric analysis (TGA) measurements were carried out. As shown in Figure 3, large weight losses were observed on the core−shell structured polymer@BT nanoparticles as compared to BT and BT-ene nanoparticles (Table 1). The TGA curves also reveal that the weight losses have the order of BT-*g*-PS3 < BT-*g*-PS1 < BT-*g*-PS2 for BT-*g*-PS (Figure 3A), and the similar order of BT-*g*-PMMA3 < BT-*g*-PMMA1 < BT-*g*-PMMA2 for BT-*g*-PMMA (Figure 3B). It can be noticed that the order of weight losses are inconsistent with the molecular weight of the grafting polymer. To further explore these phenomena, the grafting density of the core−shell structured polymer@BT nanoparticles were calculated based on the results of GPC and TGA measurements (Table 1). The results reveal that the core−shell structured nanoparticles grafted with shorter polymer chains (i.e., BT-*g*-PS1 and BT-*g*-PMMA1) have higher grafting density than those grafted with longer polymer chains (i.e., BT-*g*-PS3 and BT-*g*-PMMA3). Such results can be explained by the following two reasons. First, the longer polymer chains possess lager steric hindrance than the shorter polymer chains, which will affect the polymer chains insert into the surface of the nanoparticles. The other reason could be understood by the random coil model, in which, the thiol-terminated groups of long polymer chains have a high probability of being embedded in the polymer coil than that of short polymer chains.[55] If defining the product of molecular weight and grafting density as the surface polymer density (Table S1 in the Supporting Information), one can find that the surface polymer density values of the two types of core−shell structured nanoparticles show the order of BT-*g*-PS3 < BT-*g*-PS1 < BT-*g*-PS2 for BT-*g*-PS and the order of BT-*g*-PMMA3 < BT-*g*-PMMA1 < BT-*g*-PMMA2 for BT-*g*-PMMA, which are consistent with the TGA results.

The size of the as-received BT nanoparticles and the core−shell structured polymer@BT nanoparticles were determined by dynamic light scattering (DLS) measurements, and all samples were dispersed in toluene and sonicated for 10 min before the measurements. As shown in Figure 4A, a main peak with a large amount of nanoparticles have the average size (D_{ave}) of ∼1.2 μm was observed, which indicates the agglomeration is hard to be avoided for the as-received BT nanoparticles. However, after being grafted by polymer chains via thiol−ene click reaction, the aggregation of core−shell

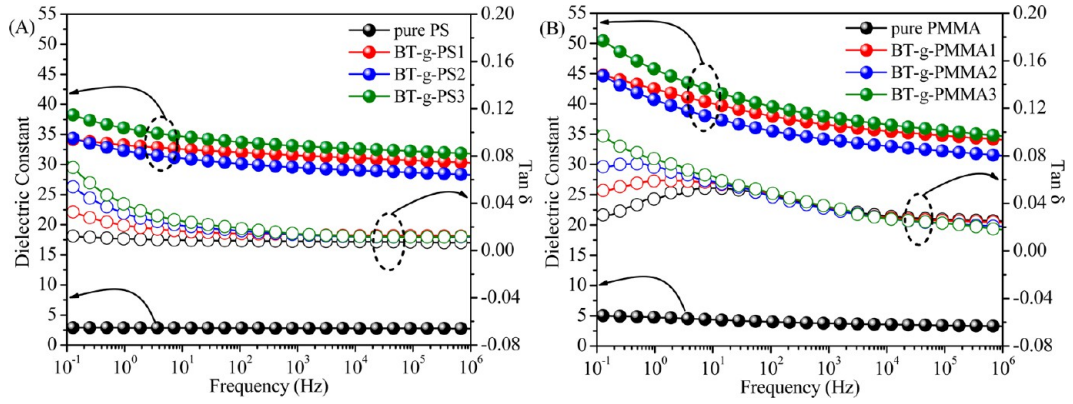

Figure 6. Frequency dependence of dielectric properties of the core−shell structured polymer@BT nanocomposites at room temperature: (A) BT-*g*-PS and (B) BT-*g*-PMMA.

structured polymer@BT nanoparticles were significantly suppressed. For instance, the D_{ave} of BT-*g*-PS2 and BT-*g*-PMMA2 were 115 ± 10 nm and 117 ± 12 nm, respectively (Figure 4B and C). These results confirm that the preparation of core−shell structured nanoparticles by thiol−ene click reaction is a promising route to suppress the aggregation of nanoparticles.

The size reduction of the nanoparticle aggregates after surface modification is further evidenced by transmission electron microscopy (TEM). Figure 5A and B present the low magnification TEM images of the as-received BT nanoparticles and BT-*g*-PS2 nanoparticles. The TEM observation vividly demonstrates that, after the introduction of polymer shell, the dispersion of the BT nanoparticles were significantly improved. The morphology of the representative core−shell structured polymer@BT nanoparticles were also illustrated by TEM (Figure 5C and D). The high magnification TEM images of BT-*g*-PS2 and BT-PMMA2 show that a stable and dense polymer shell without any noncovered sites was directly coated on the surface of the BT nanoparticles. These results further confirm that the core−shell structured polymer@BT nanoparticles have been successfully prepared.

The nanocomposite films of the core−shell structured polymer@BT nanoparticles were obtained by hot compression. The freeze-fractured cross sections of the nanocomposite films were characterized by SEM to investigate the microscopic homogeneity. Figure 5E and F present the SEM images of the BT-*g*-PS2 and BT-*g*-PMMA2 nanocomposite films, respectively. It can be observed that all the nanoparticles are coated with polymer and no agglomeration could be found. There is also no evidence of particle−matrix debonding. The SEM images of the freeze-fractured cross section in lower magnification are also provided in Figure S3 (Supporting Information); the results further confirm the well dispersion of BT nanoparticles in the nanocomposites. These results suggest that the excellent dispersion of BT nanoparticles in the polymer matrix and the very strong interfacial bonding between the BT core and the polymer shell.

Dielectric Properties of the Core−Shell Structured Polymer@BT Nanocomposites. The frequency dependence of dielectric properties of the core−shell structured polymer@BT nanocomposites were studied by a broadband dielectric spectroscopy at room temperature. As shown in Figure 6, the dielectric constant of the BT-*g*-PS and BT-*g*-PMMA nanocomposites exhibit dramatic increase in comparison with the corresponding pure polymer (i.e., PS or PMMA) over a wide range of frequency (0.1 Hz to 1 MHz). At a fixed frequency of 1 kHz, as listed in Table 2, the dielectric constant exhibits a marginal difference for the BT-*g*-PS or the BT-*g*-PMMA

Table 2. Dielectric Parameters of the Nanocomposites at 1 kHz

sample	BT content (vol %)[a]	dielectric constant[b]	dielectric loss tangent[b]
pure PS	0	2.74	0.0087
BT-*g*-PS1	58.3	31.49	0.0129
BT-*g*-PS2	56.4	29.47	0.0134
BT-*g*-PS3	59.8	33.13	0.0140
pure PMMA	0	3.69	0.0302
BT-*g*-PMMA1	58.9	36.47	0.0308
BT-*g*-PMMA2	57.1	34.01	0.0316
BT-*g*-PMMA3	60.2	37.75	0.0327

[a]Calculated from the TGA results and the density of polymers and BT nanoparticles. [b]Obtained from Figure 6.

nanocomposites. In the case of nanocomposites with the same matrix, the increase in dielectric constant of the nanocomposites mainly originates from the introduction of high dielectric constant BT nanoparticles. Therefore, the marginal difference of the dielectric constant in each type of nanocomposites should be attributed to the small difference of the BT content (Table 2).[36] For the nanocomposites with different matrix, the dielectric constant of the matrix also influences the increase of dielectric constant in the nanocomposites. Provided that the concentration of high dielectric constant particle is the same or very similar, higher dielectric constant can be expected in the nanocomposites with the matrix having the higher dielectric constant.[56] PMMA and PS have dielectric constants of 3.69 and 2.74 at 1000 Hz, respectively. This is why we observed higher dielectric constants in the PMMA nanocomposites, rather than the PS nanocomposites. It also should be noticed that, although the dielectric constant values of our nanocomposites are similar to those of composites with comparable $BaTiO_3$ volume fractions reported in most of the literature,[18−20,25−27] big difference is observed in comparison with data reported by Lin and co-workers.[57,58] It is believed that the main reason should be attributed to dielectric property difference of the $BaTiO_3$ nanoparticles used in various work. The $BaTiO_3$ nanoparticles used in most of the reported work are commercially available, while the $BaTiO_3$ nanoparticles used in refs 57 and 58 were synthesized by a unique method.

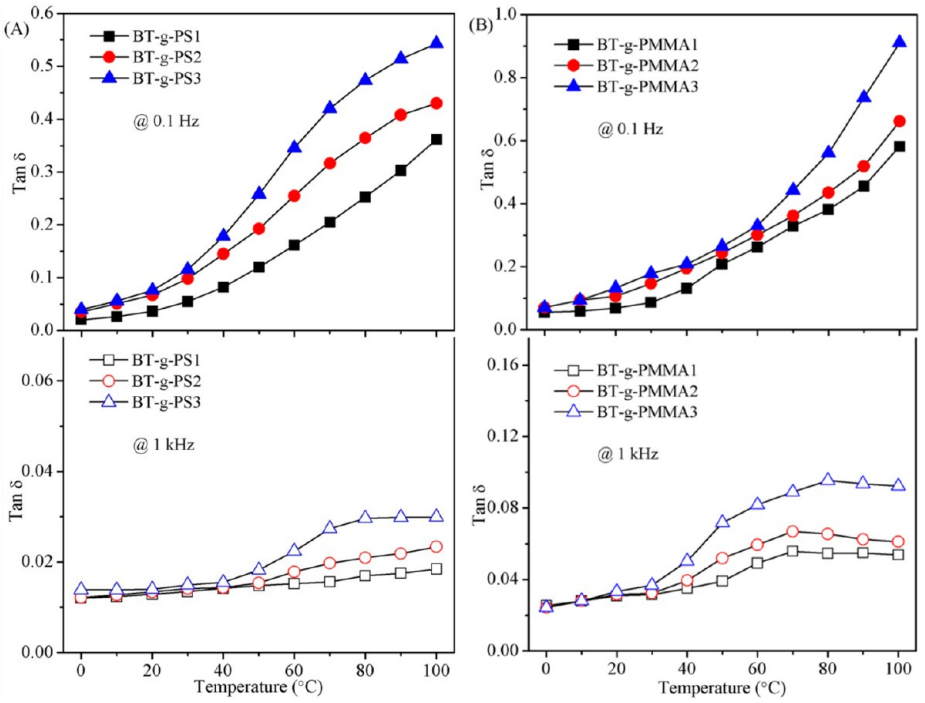

Figure 7. Temperature dependence of dielectric properties of the core−shell structured polymer@BT nanocomposites at 0.1 Hz and 1 kHz: (A) BT-*g*-PS and (B) BT-*g*-PMMA.

Figure 6 also presents the dielectric loss tangent (tan δ) of the polymer@BT nanocomposite films. It could be found that, at high frequency range (100 Hz to 1 MHz), both of the BT-*g*-PS and BT-*g*-PMMA nanocomposites exhibit similar tan δ when compared with the corresponding pure polymer (pure PS or PMMA). This is of great importance for the highly filled nanodielectric materials (>50 vol %). At the low frequency range of 0.1−100 Hz, there are marked increases of tan δ for BT-*g*-PS or BT-*g*-PMMA nanocomposites in comparison with their corresponding pure polymers. For example, the tan δ of BT-*g*-PS at 0.1 Hz is 0.0126 for pure PS, 0.0351 for BT-*g*-PS1, 0.0578 for BT-*g*-PS2, and 0.0758 for BT-*g*-PS3.

To explore the effect of temperature on the dielectric properties of the nanocomposites, Figures S4 and S5 (Supporting Information) show the frequency dependence of dielectric constant and dielectric loss of the pure polymer and nanocomposite films at different temperatures (i.e., from 0 to 100 °C). One can see that all the samples show enhanced dielectric dispersion with the increase of temperature. More interesting is that, at a given temperature and a given frequency, tan δ of both BT-*g*-PS and BT-*g*-PMMA nanocomposites is dependent on the molecular weight of the grafting polymers. To gain more clear insight, we extracted the temperature dependence of tan δ for each polymer@BT nanocomposites at 0.1 Hz and 1 kHz. As shown in Figure 7, the tan δ values of both BT-*g*-PS and BT-*g*-PMMA nanocomposites increase rapidly with the increase of temperature at 0.1 Hz and increase slowly with the increase of temperature at 1 kHz. It also should be noted that the tan δ of the two types of core−shell structured nanocomposites show the orders of BT-*g*-PS1 < BT-*g*-PS2 < BT-*g*-PS3 for BT-*g*-PS (Figure 7A) and BT-*g*-PMMA1 < BT-*g*-PMMA2 < BT-*g*-PMMA3 for BT-*g*-PMMA (Figure 7B), respectively. These characteristics become more apparent at low frequencies and high temperatures. These orders are consistent with the molecular weight of the grafting polymer, indicating that the dielectric properties of the core−shell structured polymer@BT nanocomposites are related to the molecular weight of the polymer chains and the grafting density of the core−shell structured nanoparticles.

Since Lewis introduced the concept of "nanodielectrics" in 1994,[59] extensive work has been done on the role of interface in the electrical properties of polymer nanocomposites. It has been well-known that the nanometric interface is one of the most important factors determining the dielectric properties of nanodielectrics.[60−65] Regarding our core−shell structured polymer@BT nanocomposites, the polymer shell, which is robust anchored onto the surface of BT core via thiol−ene click reaction, not only plays the role of interface but also is directly used as the matrix of the final nanocomposites. In such a case, the interfaces of the polymer@BT nanocomposites are mainly dependent on the grafting density of the polymer chains. Considering that the grafting density is closely associated with the molecular weight of the grafting polymer,[66,67] we suggest a scheme showing the relationship between the molecular weight of the grafting polymer and the grafting density of the core−shell structured nanoparticles. As illustrated in Figure 8, the polymer chains grafted on the surface of nanoparticles have a "brush-to-mushroom" transition and the grafting density decrease as the molecular weight of the grafting polymer increases.[68] For example, the grafting polymer chains with the lowest molecular weight result in the highest grafting density, in which the polymer chains are unperturbed and exhibit a "brush" formation (Figure 8A). With the further increase of the molecular weight of the grafting polymer, the grafting density tapers off and the polymer chains begin to curl (Figure 8B). Eventually, the polymer chains will become a "mushroom" formation, and only a few polymer chains could be anchored on the surface of nanoparticles because of the steric hindrance effect (Figure 8C). Accordingly, in our core−shell structured polymer@BT nanocomposites, the difference of the dielectric

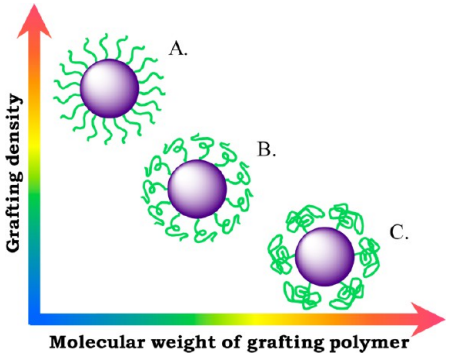

Figure 8. Schematic illustration for the relationship between the molecular weight of grafting polymer and grafting density of the core–shell structured nanoparticles.

properties can be understood by the following explanation: For the BT-*g*-PS1 or BT-*g*-PMMA1 nanocomposites, the molecular weight of the grafting polymer is the lowest and the grafting density is the highest (see Table 1), thus most of polymer matrix are anchored on the surface of BT nanoparticles and the movement of the polymer segment could be restricted, namely the interface in the corresponding nanocomposites is compacted. In this case, the space charge polarization, which is an important factor causing low frequency dielectric loss, is suppressed. However, in the BT-*g*-PS3 or BT-*g*-PMMA3 nanocomposites, the grafting density is the lowest and the grafting polymer possess the highest molecular weight, it means only a small fraction of polymer matrix are bonded on the BT and most of polymer segment can move easily, which leads to relatively loose interface and thus strong space charge polarization in the corresponding nanocomposites. These results prove that the dielectric properties of the core–shell structured polymer@BT nanocomposites are closely related to the molecular weight of the polymer chains and the grafting density of the core–shell structured nanoparticles.

Energy Storage Capability of the Core–Shell Structured Polymer@BT Nanocomposites. Generally, the energy densities of the dielectric materials can be calculated from the electric displacement–electric field (D–E) loops using the following integral:[5]

$$U_e = \int E \, dD \tag{1}$$

where E is the electric field and D is the electric displacement. To investigate the energy storage capability of the core–shell structured polymer@BT nanocomposites, the D–E loops were measured at various electric fields. As shown in Figure 9A and B, the electric displacement of the nanocomposites exhibit markedly increases in comparison with the corresponding pure polymer (i.e., PS or PMMA), which is mainly attributed to the increase of dielectric constant of the nanocomposites. It also should be noticed that, the BT-*g*-PS nanocomposites exhibit narrower D–E loops and lower remnant polarizations than the BT-*g*-PMMA nanocomposites. This is result of the lower dipole polarization and dielectric loss of PS in comparison with PMMA. The discharged energy densities of the core–shell structured polymer@BT nanocomposites determined from D–E loops were calculated according to eq 1 and summarized in Figure 9C and D. One can see that the energy densities increase with increasing of the electric field. Of interest is that, compared with the BT-*g*-PMMA nanocomposites, the energy densities of the BT-*g*-PS nanocomposites almost show a linear

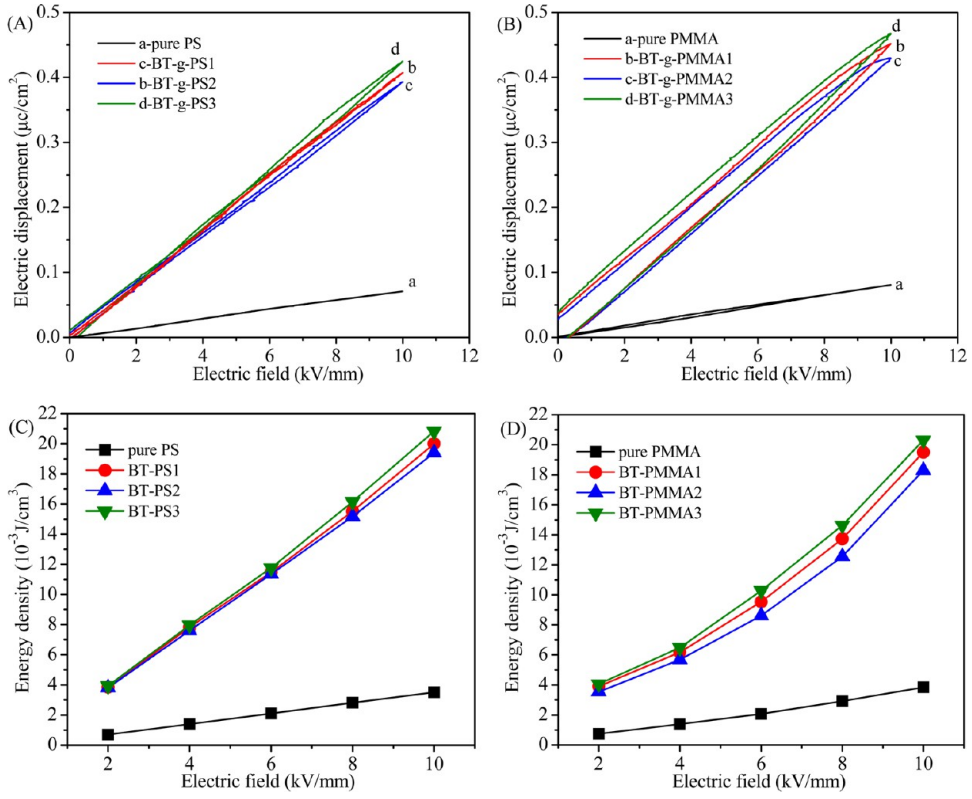

Figure 9. Electric displacement–electric field (D–E) loops of the core–shell structured polymer@BT nanocomposites (A) BT-*g*-PS and (B) BT-*g*-PMMA. Energy densities of the core–shell structured polymer@BT nanocomposites (C) BT-*g*-PS and (D) BT-*g*-PMMA.

dx.doi.org/10.1021/am4048267 | ACS Appl. Mater. Interfaces 2014, 6, 1812–1822

enhancement as the electric field increases. This result can be understood by the remnant polarizations of the nanocomposites. Compared with the BT-*g*-PS nanocomposites, the BT-*g*-PMMA nanocomposites show the high remnant polarization, which results in a reduction of the integrated area of the *D*−*E* loops and thus reduced discharging energy.[7,69] Because of the superlow dielectric loss, U_e can be roughly calculated by the following equation

$$U_e = \frac{1}{2}\varepsilon_0 \varepsilon E^2 \quad (2)$$

where ε_0 and ε are the dielectric constants of free space and the nanocomposites, respectively. According to eq 2, U_e versus E should display a quadratic relationship. However, U_e versus E in Figure 9C looks like a linear relationship. This is mainly attributed to the low measuring electric fields. At higher electric fields, a quadratic relationship can be expected.

For practical application, the energy efficiency is an important parameter used to evaluate the energy storage capability of the dielectric materials, which is defined as the ratio of discharged energy density to charged energy density. Thus, dielectric materials with high discharged energy density and high energy efficiency are highly desirable. Figure 10 gives

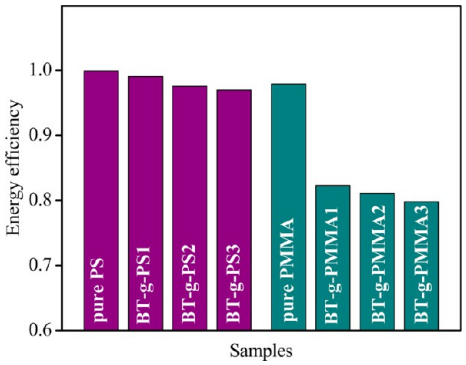

Figure 10. Energy efficiency of the core−shell structured polymer@BT nanocomposites under the electric field of 10 kV/mm.

the energy efficiency for core−shell structured polymer@BT nanocomposites under the electric field of 10 kV/mm. It can be seen that (i) all nanocomposites remain relatively high energy efficiency (i.e, > 80%); (ii) compared with the BT-*g*-PMMA nanocomposites, BT-*g*-PS nanocomposites exhibit much higher energy efficiency because of the lower remnant polarizations. More interestingly, the order of energy efficiency of each nanocomposites exhibit the same dependence on the grafting density of the core−shell structured nanoparticles. In other words, the energy storage capability of the core−shell structured polymer@BT nanocomposites is also closely associated to the molecular weight of the polymer chains and the grafting density of the core−shell structured nanoparticles. That is to say, both polymer molecular weight and grafting density, which have not been considered in previous research, also are important factors which should be considered when designing core−shell structured polymer nanocomposites with high energy density and high energy efficiency.

CONCLUSION

In summary, using a combination of RAFT polymerization and thiol−ene click reaction, a series of core−shell structured polymer@BT nanocomposites with excellent dielectric properties were successfully prepared. Thiol-terminated polymer chains with three different molecular weights were adopted for the preparation of both BT-*g*-PS and BT-*g*-PMMA, resulting in different grafting densities of the corresponding core−shell structured nanoparticles. Dielectric measurements revealed that the dielectric constant of all the BT-*g*-PS and BT-*g*-PMMA nanocomposites were significantly enhanced when compared with the corresponding pure polymer, and the dielectric loss were still maintained in a relatively low level in a wide range of frequency. The temperature dependence of dielectric properties of BT-*g*-PS and BT-*g*-PMMA nanocomposites demonstrated that higher dielectric loss could only be observed in the low frequency range/high temperature range because of the interfacial polarization. Additionally, the energy storage capabilities of the core−shell structured polymer@BT nanocomposites were also investigated and the results revealed that all nanocomposites have relatively high energy efficiency (i.e., >80%). More importantly, this work also provides clear insights into understanding the relationship among the dielectric properties and the energy storage capability of the core−shell structured polymer@BT nanocomposites, the molecular weight of the polymer chains, and the grafting density of the core−shell structured nanoparticles. We believe that the combination of RAFT polymerization and thiol−ene click reaction could be a promising "grafting to" route to prepare high-performance nanodielectric materials used in energy storage devices.

ASSOCIATED CONTENT

Supporting Information

XRD pattern and HR-TEM image of BT nanoparticles, FT-IR spectra of the PS1 before and after aminolysis, surface polymer density of the nanoparticles, SEM images of the freeze-fractured cross section of the nanocomposite films in lower magnification, and the Dielectric properties of the nanocomposites under the temperature from 0 to 100 °C. This material is available free of charge via the Internet at http://pubs.acs.org.

AUTHOR INFORMATION

Corresponding Authors

*E-mail: xyhuang@sjtu.edu.cn (X.Y.H.).
*E-mail: pkjiang@sjtu.edu.cn (P.K.J.).

Notes

The authors declare no competing financial interest.

ACKNOWLEDGMENTS

The authors gratefully acknowledge support from the National Science Foundation of China (Nos. 51107081, 51217117), the Research Fund for the Doctoral Program of Higher Education (Grant Nos. 20100073120038, 20120073110031), the Shanghai Leading Academic Discipline Project (Grant No. B202), and the Special Fund of the National Priority Basic Research of China under Grant 2014CB239503. This work was also supported by the State Key Lab. of Power System.

REFERENCES

(1) Dang, Z. M.; Yuan, J. K.; Yao, S. H.; Liao, R. J. *Adv. Mater.* **2013**, *25*, 6334−6365.
(2) Brochu, P.; Pei, Q. B. *Macromol. Rapid Commun.* **2010**, *31*, 10−36.
(3) Ortiz, R. P.; Facchetti, A.; Marks, T. J. *Chem. Rev.* **2010**, *110*, 205−239.
(4) Wang, Y.; Zhou, X.; Chen, Q.; Chu, B. J.; Zhang, Q. M. *IEEE Trans. Dielectr. Electr. Insul.* **2010**, *17*, 1036−1042.

(5) Chu, B.; Zhou, X.; Ren, K.; Neese, B.; Lin, M.; Wang, Q.; Bauer, F.; Zhang, Q. M. *Science* **2006**, *313*, 334−336.
(6) Hardy, C. G.; Islam, M. S.; Gonzalez-Delozier, D.; Ploehn, H. J.; Tang, C. B. *Macromol. Rapid Commun.* **2012**, *33*, 791−797.
(7) Hardy, C. G.; Islam, M. S.; Gonzalez-Delozier, D.; Morgan, J. E.; Cash, B.; Benicewicz, B. C.; Ploehn, H. J.; Tang, C. B. *Chem. Mater.* **2013**, *25*, 799−807.
(8) Thakur, V. K.; Tan, E. J.; Lin, M. F.; Lee, P. S. *Polym. Chem.* **2011**, *2*, 2000−2009.
(9) Dang, Z. M.; Yuan, J. K.; Zha, J. W.; Zhou, T.; Li, S. T.; Hu, G. H. *Prog. Mater. Sci.* **2012**, *57*, 660−723.
(10) Wang, Q.; Zhu, L. *J. Polym. Sci., Part B: Polym. Phys.* **2011**, *49*, 1421−1429.
(11) Li, J.; Claude, J.; Norena-Franco, L. E.; Seok, S. I.; Wang, Q. *Chem. Mater.* **2008**, *20*, 6304−6306.
(12) Dang, Z. M.; Zhou, T.; Yao, S. H.; Yuan, J. K.; Zha, J. W.; Song, H. T.; Li, J. Y.; Chen, Q.; Yang, W. T.; Bai, J. B. *Adv. Mater.* **2009**, *21*, 2077−2082.
(13) Li, J.; Seok, S. I.; Chu, B.; Dogan, F.; Zhang, Q.; Wang, Q. *Adv. Mater.* **2009**, *21*, 217−221.
(14) Li, J.; Khanchaitit, P.; Han, K.; Wang, Q. *Chem. Mater.* **2010**, *22*, 5350−5357.
(15) Zhang, Y.; Wang, Y.; Deng, Y.; Li, M.; Bai, J. B. *ACS Appl. Mater. Interfaces* **2012**, *4*, 65−68.
(16) Wu, W.; Huang, X. Y.; Li, S. T.; Jiang, P. K.; Toshikatsu, T. *J. Phys. Chem. C* **2012**, *116*, 24887−24895.
(17) Xie, L. Y.; Huang, X. Y.; Li, B. W.; Zhi, C. Y.; Tanaka, T.; Jiang, P. K. *Phys. Chem. Chem. Phys.* **2013**, *15*, 17560−17569.
(18) Zhou, T.; Zha, J. W.; Cui, R. Y.; Fan, B. H.; Yuan, J. K.; Dang, Z. M. *ACS Appl. Mater. Interfaces* **2011**, *3*, 2184−2188.
(19) Song, Y.; Shen, Y.; Liu, H. Y.; Lin, Y. H.; Li, M.; Nan, C. W. *J. Mater. Chem.* **2012**, *22*, 8063−8068.
(20) Kim, P.; Doss, N. M.; Tillotson, J. P.; Hotchkiss, P. J.; Pan, M. J.; Marder, S. R.; Li, J.; Calame, J. P.; Perry, J. W. *ACS Nano* **2009**, *3*, 2581−2592.
(21) Almadhoun, M. N.; Bhansali, U. S.; Alshareef, H. N. *J. Mater. Chem.* **2012**, *22*, 11196−11200.
(22) Li, Y.; Huang, X. Y.; Hu, Z. W.; Jiang, P. K.; Li, S. T.; Tanaka, T. *ACS Appl. Mater. Interfaces* **2011**, *3*, 4396−4403.
(23) Subodh, G.; Deepu, V.; Mohanan, P.; Sebastian, M. T. *Appl. Phys. Lett.* **2009**, *95*, 062903.
(24) Maliakal, A.; Katz, H.; Cotts, P. M.; Subramoney, S.; Mirau, P. *J. Am. Chem. Soc.* **2005**, *127*, 14655−14662.
(25) Xie, L. Y.; Huang, X. Y.; Huang, Y. H.; Yang, K.; Jiang, P. K. *ACS Appl. Mater. Interfaces* **2013**, *5*, 1747−1756.
(26) Xie, L. Y.; Huang, X. Y.; Huang, Y. H.; Yang, K.; Jiang, P. K. *J. Phys. Chem. C* **2013**, *117*, 22525−22537.
(27) Guo, N.; DiBenedetto, S. A.; Tewari, P.; Lanagan, M. T.; Ratner, M. A.; Marks, T. J. *Chem. Mater.* **2010**, *22*, 1567−1578.
(28) Li, Z.; Fredin, L. A.; Tewari, P.; DiBenedetto, S. A.; Lanagan, M. T.; Ratner, M. A.; Marks, T. J. *Chem. Mater.* **2010**, *22*, 5154−5164.
(29) Shen, Y.; Lin, Y. H.; Li, M.; Nan, C. W. *Adv. Mater.* **2007**, *19*, 1418−1422.
(30) Jung, H. M.; Kang, J. H.; Yang, S. Y.; Won, J. C.; Kim, Y. S. *Chem. Mater.* **2010**, *22*, 450−456.
(31) Balasubramanian, B.; Kraemer, K. L.; Reding, N. A.; Skomski, R.; Ducharme, S.; Sellmyer, D. J. *ACS Nano* **2010**, *4*, 1893−1900.
(32) Fredin, L. A.; Li, Z.; Ratner, M. A.; Lanagan, M. T.; Marks, T. J. *Adv. Mater.* **2012**, *24*, 5946−5953.
(33) Fredin, L. A.; Li, Z.; Lanagan, M. T.; Ratner, M. A.; Marks, T. J. *Adv. Funct. Mater.* **2013**, *23*, 3560−3569.
(34) Xie, L. Y.; Huang, X. Y.; Wu, C.; Jiang, P. K. *J. Mater. Chem.* **2011**, *21*, 5897−5906.
(35) Yang, K.; Huang, X. Y.; Xie, L. Y.; Wu, C.; Jiang, P. K.; Tanaka, T. *Macromol. Rapid Commun.* **2012**, *33*, 1921−1926.
(36) Yang, K.; Huang, X. Y.; Huang, Y. H.; Xie, L. Y.; Jiang, P. K. *Chem. Mater.* **2013**, *25*, 2327−2338.
(37) Tchoul, M. N.; Fillery, S. P.; Koerner, H.; Drummy, L. F.; Oyerokun, F. T.; Mirau, P. A.; Durstock, M. F.; Vaia, R. A. *Chem. Mater.* **2010**, *22*, 1749−1759.
(38) Lowe, A. B. *Polym. Chem.* **2010**, *1*, 17−36.
(39) Hoyle, C. E.; Bowman, C. N. *Angew. Chem., Int. Ed.* **2010**, *49*, 1540−1573.
(40) Dondoni, A.; Marra, A. *Chem. Soc. Rev.* **2012**, *41*, 573−586.
(41) Shih, H.; Fraser, A. K.; Lin, C. C. *ACS Appl. Mater. Interfaces* **2013**, *5*, 1673−1680.
(42) Lluch, C.; Ronda, J. C.; Galiá, M.; Lligadas, G.; Cádiz, V. *Biomacromolecules* **2010**, *11*, 1646−1653.
(43) Sumerlin, B. S.; Vogt, A. P. *Macromolecules* **2009**, *43*, 1−13.
(44) Hoyle, C. E.; Lowe, A. B.; Bowman, C. N. *Chem. Soc. Rev.* **2010**, *39*, 1355−1387.
(45) Tedja, R.; Soeriyadi, A. H.; Whittaker, M. R.; Lim, M.; Marquis, C.; Boyer, C.; Davis, T. P.; Amal, R. *Polym. Chem.* **2012**, *3*, 2743−2751.
(46) Tingaut, P.; Hauert, R.; Zimmermann, T. *J. Mater. Chem.* **2011**, *21*, 16066−16076.
(47) Sparks, B. J.; Hoff, E. F. T.; Xiong, L.; Goetz, J. T.; Patton, D. L. *ACS Appl. Mater. Interfaces* **2013**, *5*, 1811−1817.
(48) Convertine, A. J.; Lokitz, B. S.; Vasileva, Y.; Myrick, L. J.; Scales, C. W.; Lowe, A. B.; McCormick, C. L. *Macromolecules* **2006**, *39*, 1724−1730.
(49) Shen, W. Q.; Qiu, Q. A.; Wang, Y.; Miao, M. A.; Li, B. S.; Zhang, T. S.; Cao, A. N.; An, Z. S. *Macromol. Rapid Commun.* **2010**, *31*, 1444−1448.
(50) Roy, D.; Ghosn, B.; Song, E. H.; Ratner, D. M.; Stayton, P. S. *Polym. Chem.* **2013**, *4*, 1153−1160.
(51) Roth, P. J.; Boyer, C.; Lowe, A. B.; Davis, T. P. *Macromol. Rapid Commun.* **2011**, *32*, 1123−1143.
(52) Lu, L. C.; Zhang, H. J.; Yang, N. F.; Cai, Y. L. *Macromolecules* **2006**, *39*, 3770−3776.
(53) Zhang, H. J.; Deng, J. J.; Lu, L. C.; Cai, Y. L. *Macromolecules* **2007**, *40*, 9252−9261.
(54) Willcock, H.; O'Reilly, R. K. *Polym. Chem.* **2010**, *1*, 149−157.
(55) Natarajan, B.; Neely, T.; Rungta, A.; Benicewicz, B. C.; Schadler, L. S. *Macromolecules* **2013**, *46*, 4909−4918.
(56) Xu, J. W.; Wong, C. P. *J. Electr. Mater.* **2006**, *35*, 1087−1094.
(57) Guo, H. Z.; Mudryk, Y.; Ahmad, M. I.; Pang, X. C.; Zhao, L.; Akinc, M.; Pecharsky, V. K.; Bowler, N.; Lin, Z. Q.; Tan, X. *J. Mater. Chem.* **2012**, *22*, 23944−23951.
(58) Pang, X. C.; He, Y. J.; Jiang, B. B.; Iocozzia, J.; Zhao, L.; Guo, H. Z.; Liu, J.; Akinc, M.; Bowler, N.; Tan, X. L.; Lin, Z. Q. *Nanoscale* **2013**, *5*, 8695−8702.
(59) Lewis, T. *J. IEEE Trans. Dielectr. Electr. Insul.* **1994**, *1*, 812−825.
(60) Lewis, T. *J. IEEE Trans. Dielectr. Electr. Insul.* **2004**, *11*, 739−753.
(61) Tanaka, T.; Kozako, M.; Fuse, N.; Ohki, Y. *IEEE Trans. Dielectr. Electr. Insul.* **2005**, *12*, 669−681.
(62) Roy, M.; Nelson, J. K.; MacCrone, R. K.; Schadler, L. S.; Reed, C. W.; Keefe, R.; Zenger, W. *IEEE Trans. Dielectr. Electr. Insul.* **2005**, *12*, 629−643.
(63) Schadler, L. S. *Nat. Mater.* **2007**, *6*, 257−258.
(64) Wang, D.; Bao, Y.; Zha, J.-W.; Zhao, J.; Dang, Z. M.; Hu, G. H. *ACS Appl. Mater. Interfaces* **2012**, *4*, 6273−6279.
(65) Siddabattuni, S.; Schuman, T. P.; Dogan, F. *ACS Appl. Mater. Interfaces* **2013**, *5*, 1917−1927.
(66) Oyerokun, F. T.; Vaia, R. A. *Macromolecules* **2012**, *45*, 7649−7659.
(67) Kumar, S. K.; Jouault, N.; Benicewicz, B.; Neely, T. *Macromolecules* **2013**, *46*, 3199−3214.
(68) Dukes, D.; Li, Y.; Lewis, S.; Benicewicz, B.; Schadler, L. S.; Kumar, S. K. *Macromolecules* **2010**, *43*, 1564−1570.
(69) Wu, S.; Li, W.; Lin, M.; Burlingame, Q.; Chen, Q.; Payzant, A.; Xiao, K.; Zhang, Q. M. *Adv. Mater.* **2013**, *25*, 1734−1738.